



ORIGINAL RESEARCH ARTICLE

# Effect of Aging Treatment Temperature on Microstructure and Properties of Al-9.3Si-0.41Mg-0.2Zr-0.01Sr-0.08Ti-0.2Ce Cast Aluminum Alloy

Qin Wang, Qingshan Zhou, Lele Liu, and Xiaojing Xu

Submitted: 4 January 2024 / Revised: 13 May 2024 / Accepted: 24 May 2024

In this paper, the influence of three aging temperatures (165, 175, and 185 °C) under identical aging time (6 h) on the microstructure and properties of Al-9.3Si-0.41 Mg-0.2Zr-0.01Sr-0.08Ti-0.2Ce casting aluminum alloy was investigated. As the aging temperature raised from 165 to 185 °C, the alloy exhibited finer microstructure evolution, transitioning from primarily GP zones to  $\beta''$  phase,  $\beta'$  phase (Metastable phase), and ultimately  $\beta$  ( $\text{Mg}_2\text{Si}$ ) phase (Stable phase). The strengthening effect due to dislocations initially increased and then diminished. Mechanical property tests indicated that with the elevation of aging temperature, the alloy's tensile strength and hardness demonstrate a trend of initially rising and then declining due to the effective strengthening effect of  $\beta''$  phase. The maximum tensile strength reached 288.78 MPa, the maximum yield strength was 259.38 MPa, and the maximum hardness was 118.89 HV. Additionally, alloy samples aged for 6 h at 175 °C displayed discontinuously distributed grain boundary precipitates, exhibiting good electrical conductivity and corrosion resistance.

**Keywords** Al-Si-Mg alloy, aging treatment, electrical conductivity, mechanical properties

## 1. Introduction

Aluminum-Silicon-Magnesium (Al-Si-Mg) alloys are widely utilized in various sectors such as transportation, automotive, aerospace, and defense industries owing to their excellent casting properties, high tensile, and fatigue strengths, as well as superior corrosion resistance (Ref 1). In recent years, the main trend has been to achieve low-cost, high-performance Al-Si-Mg alloys due to their widespread usage in casting aluminum alloys. The properties of Al-Si-Mg alloys depend on their composition and processing parameters, where aging treatment can effectively enhance the overall performance of these alloys.

Aging treatment plays a role in adjusting the type, size, and quantity of precipitates within the  $\alpha$ -Al matrix, thereby altering the strength and hardness of Al-Si-Mg casting aluminum alloys (Ref 1). Based on the phase transformation sequence during aging treatment under the influence of temperature and time, the precipitation sequence in Al-Si-Mg alloys is delineated as follows: SSS (Supersaturated Solid Solution)  $\rightarrow$  Atomic Clusters  $\rightarrow$  Guinier-Preston (GP) zones (Spherical)  $\rightarrow$   $\beta''$

(Needle-like)  $\rightarrow$   $\beta'$  (Rod-like) + Si  $\rightarrow$   $\beta$  ( $\text{Mg}_2\text{Si}$ ) + Si (Ref 1-3). Among these phases, the most effective strengthening phase is the needle-like metastable  $\beta''$  phase (Ref 4), whereas the over-aging phases,  $\beta'$  and  $\beta$  ( $\text{Mg}_2\text{Si}$ ), can lead to a reduction in alloy hardness. The relationship between these precipitates and alloy performance remains a focal point of research. Studies (Ref 4-6) indicated that artificial aging results in higher cluster density and average size compared to natural aging. Sha et al. (Ref 7) found that the hardness and maximum tensile strength of Al-7Si-Mg alloy peaked after aging at 180 °C for 4 h, although elongation decreased due to higher  $\beta''$  phase density. Ammar et al. (Ref 8) investigated the impact of aging temperature and time on the tensile properties and quality indices of Al-9%Si-0.5%Mg cast alloy. They found that the alloy reached peak strength after aging for 24 h at 170 °C, 1 h at 195 °C, 30 min at 220 °C, and 10 min at 245 °C, while high-temperature aging treatment led to a decline in the tensile properties and quality indices of the castings. Kang et al. (Ref 9) investigated the Al-Si-Mg alloys after the solid solution heat treatment at 520 °C for 90 min. They found that the YS and UTS values increased, while the EL decreased in comparison with those of the solution heat-treated only Al-Mg-Si alloys. And the maximum YS and UTS values were obtained after subjecting the alloy to aging heat treatment at 180 °C for 180 min. Yang et al. (Ref 10) investigated the microstructure evolution of 6082 aluminum alloy at different artificial aging temperatures. It was found that with increasing artificial aging temperatures, the hardness value of the sample first increased and then decreased, reaching a peak at aged 200 °C for 1 h.

Consequently, the microstructural properties of Al-9Si-Mg casting alloys at high-temperature aging temperatures ranging from 180 to 245 °C have been a significant research focus. However, there has been limited research on the microstructural

Qin Wang, Qingshan Zhou, Lele Liu, and Xiaojing Xu, Institute of Advanced Manufacturing and Modern Equipment Technology, Jiangsu University, Zhenjiang 212013, China. Contact e-mail: yjs\_xx@126.com.

properties at lower aging temperatures from 165 to 185 °C. Hence, this experiment aims to explore the effects of different aging temperatures (165, 175, and 185 °C) on the microstructure and properties of Al-9Si-0.4Mg-Sr-Zr-Ti-Ce casting aluminum alloys. A systematic characterization of the microstructure, mechanical properties, and corrosion resistance of alloy specimens at different aging temperatures has been conducted to directly assess the influence of lower aging temperatures on alloy properties, aiding in more effectively improving alloy performance. Additionally, this study uncovered the impact of aging temperatures in this range on the electrical conductivity of Al-9Si-0.4Mg-Sr-Zr-Ti-Ce casting aluminum alloys.

## 2. Experimental Procedure

The specific process for preparing the alloy specimens used in this experiment is as follows: (1) Al (99.97wt%), intermediate alloy of Al-20 wt.%Si, Al-4.11 wt.%Zr, Al-5.11 wt.%Ti-B were placed into a graphite crucible, which was then heated in an SG20 bell-type resistance melting furnace to 900 °C. The alloy was kept molten for 1 h after reaching the designated temperature; (2) after the insulation period, the furnace temperature was reduced to 850 °C, and 10 g of C<sub>2</sub>Cl<sub>6</sub>, wrapped in tin foil, was added for degassing. Stirring was continued until no gas was released, followed by a 15-min standing period; (3) Al-9.89 wt.%Sr intermediate alloy was added and stirred uniformly, then incubated for 2 h; (4) the temperature was lowered to 750 °C, pure 99.98 wt.% magnesium blocks were added, stirred uniformly, and allowed to stand for 15 min at a constant temperature; (5) Al-20 wt.%Ce intermediate alloy was added, thoroughly stirred, and allowed to stand for 15 min; (6) C<sub>2</sub>Cl<sub>6</sub> was added, stirred until no gas was released, and then allowed to stand for 15 min. After the temperature dropped to 700 °C, the crucible was removed to remove slag, and the molten alloy was poured into preheated molds (400 °C). After cooling, the molds were opened to extract the castings.

Upon testing, the actual composition of the samples was determined to be Al-9.3Si-0.41Mg-0.2Zr-0.01Sr-0.08Ti-0.2Ce. The samples underwent the same solution treatment (540 °C × 4 h), followed by quenching. After cooling, three different aging treatments were conducted on the samples, with specific solution and aging treatment parameters detailed in Table 1.

After heat treatment, samples measuring 8 × 8 × 8 mm underwent hardness and electrical conductivity tests. Surface hardness was measured using the HV-1000 hardness tester (300 gf load force and 15 s loading time), and the hardness value of each sample was obtained as the average from five readings. Electrical conductivity tests were conducted using the 7501 A eddy current conductivity meter. Prior to the experiment, the high and low values of the eddy current conductivity meter needed calibration. The microstructure and fracture morphology of the samples was performed using a JEOL JSM-IT300 scanning electron microscope (SEM) operating at a working voltage of 20 kV. X-ray diffraction analysis of the phase composition was conducted using the XRD-6100 Lab x-ray diffractometer (wavelength of 0.15406 nm, scanning speed of 5°/min), with semi-peak width and fitting curves of the samples plotted using Jade and Origin software. Thin slices

**Table 1 The specific solution and aging treatment parameters**

| Samples | Solid solution system | Aging system |
|---------|-----------------------|--------------|
| 1#      | 540 °C × 4 h          | 165 °C × 6 h |
| 2#      | ...                   | 175 °C × 6 h |
| 3#      | ...                   | 185 °C × 6 h |

measuring 8 × 8 × 0.5 mm were obtained from the castings using wire cutting. The samples were thinned artificially to 0.1 mm and then ion-thinned. Circular pieces of φ3 mm were extracted from the thinned samples and observed in the FEI Talos F200X field emission transmission electron microscope to analyze the precipitation phase within the grains and at grain boundaries. Tensile testing was performed using the WDW-200G testing machine at a speed of 1 mm/min, and He elongation at fracture was calculated after completion of the test. For intergranular corrosion experiments, cuboid samples measuring 8 × 8 × 6 mm were immersed in a 10% NaOH solution for 10 min, followed by immersion in a 30% HNO<sub>3</sub> solution for about 5 s. Subsequently, the samples were soaked in a corrosion solution of NaCl 57 g/L + H<sub>2</sub>O<sub>2</sub> 10 ml/L for 6 h at 35 °C, and the corrosion depth was observed using an optical microscope (OM) model 4XC-MS after embedding, polishing, and etching according to GB/T7998-2005 to determine the corrosion grade. The dissolution ratio of the stripping corrosion solution was 64 mol/cm<sup>2</sup>, and the corrosion solution ratio was 4.0 mol/L NaCl + 0.5 mol/L KNO<sub>3</sub> + 0.1 mol/L HNO<sub>3</sub>. After the corrosion process, the samples were cleaned by ultrasonic agitation in water, soaked in HNO<sub>3</sub> for 30 s, dried, observed under a stereomicroscope, and the corrosion grade was determined according to GB/T22639-2022 for analysis of the anti-stripping corrosion performance. Electrochemical measurements were conducted using the CH Instruments chi-760e electrochemical workstation connected to three electrodes (working electrode, saturated calomel electrode as the reference electrode, and platinum plate as the counter electrode). The electrolyte used was 3.5 wt.% NaCl (0.6 M). During the electrochemical testing process, the aluminum alloy samples were exposed to an electrolyte area of 1 cm<sup>2</sup>, with a potential scan rate of 1 mV/s. After completing the electrochemical tests, CVIEW2 software was used to analyze the corrosion potential and polarization curves of the alloy samples.

## 3. Results and Discussion

### 3.1 SEM Analysis

Figure 1 displays the microstructure morphology observed under the SEM after subjecting to three different aging treatments. Comparing Fig. 1(b), (d), and (e), it was evident that in comparison with sample 1#, samples 2# and 3# exhibit finer and more numerous black spherical precipitates. In the artificial aging process of the Al-Si-Mg alloy, small Si-rich clusters were first formed, followed by a coarsening process. Mg-rich clusters began to form and grow near surviving Si-rich clusters (Ref 11). Mg atoms and Si-rich clusters tended to form co-clusters, constituting very fine disordered solute aggregates (Ref 10). The small, black microstructure was observed in the

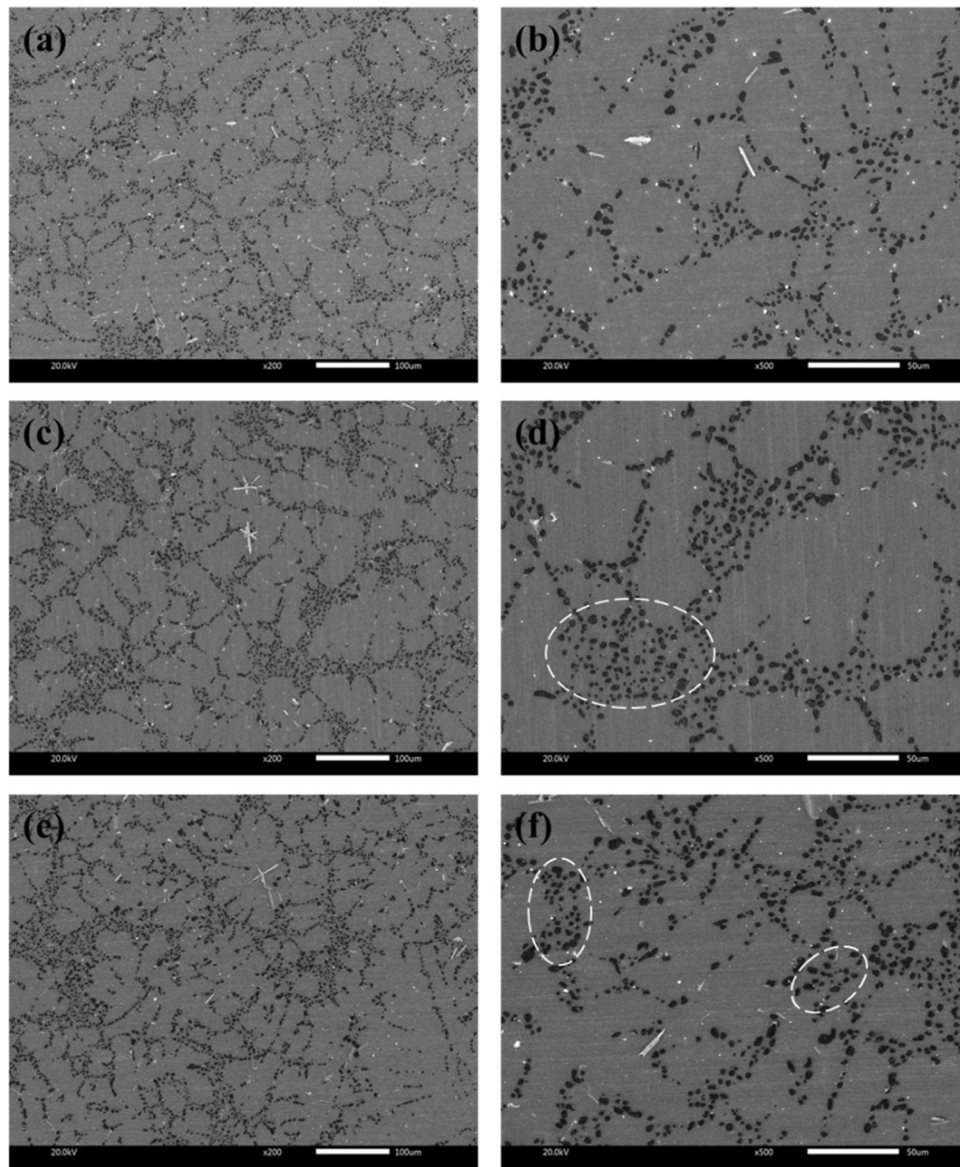


**Fig. 1** SEM diagram of alloy specimens with different aging treatments: (a, b) 1#; (c, d) 2#; and (e, f) 3#

figures that likely represent these Si clusters and Mg-Si co-clusters as precipitates. Under similar aging times, an increase in aging temperature stimulated atomic diffusion, accelerating the precipitation process, which potentially led to an increased quantity of these Mg-Si-rich clusters. However, the aggregated growth of the precipitates marked in the enclosed areas in the figures could unfavorably impacted the mechanical properties of the alloy.

### 3.2 XRD Analysis

Figure 2 illustrates the x-ray diffraction (XRD) patterns and the full-width at half-maximum (FWHM) charts of the alloy samples after three different temperature aging treatments, along with the linear fitting relationships of  $(\delta 2\theta)^2/\tan^2\theta_0$  and  $\delta 2\theta/\tan\theta_0\sin\theta_0$ . Figure 2(a), (c), and (e) displays the XRD patterns of samples 1#, 2#, and 3#. Post aging treatments, the XRD patterns of the Al-9.3Si-0.41Mg-0.2Zr-0.01Sr-0.08Ti-0.2Ce aluminum alloy revealed abundant diffraction peaks of Al, along with a minor presence of the  $\beta$  phase ( $Mg_2Si$ ) and Si.

Owing to the coherent structure between the GP zones and the matrix, their crystallographic characteristics were indistinguishable and thus not observed in the XRD patterns. Therefore, the aged Al-9Si-0.41Mg alloy primarily consisted of  $\alpha$ -Al matrix,  $\beta$  phase ( $Mg_2Si$ ), and elemental Si (Ref 1). Fig. 2(b), (d), and (f) represents the FWHM charts of the three samples. Compared to the standard FWHM of pure Al, all samples exhibited noticeable alterations in both high- and low-angle FWHM. Comparative analysis of the FWHM charts among the three samples indicated that the overall FWHM of sample 3# is lower than that of samples 1# and 2#, implying inferior crystallinity in sample 3# in contrast to samples 1# and 2#. The larger grain size in sample 3# suggested a coarser yet more uniform crystalline structure, depicting a trend of grain growth within the alloy with increasing aging temperature.

Through the Williamson–Hall model, the half-width of the diffraction peaks of the 1#, 2#, and 3# alloy samples was processed to estimate the dislocation density and average lattice strain of the three alloys, thereby calculating the dislocation

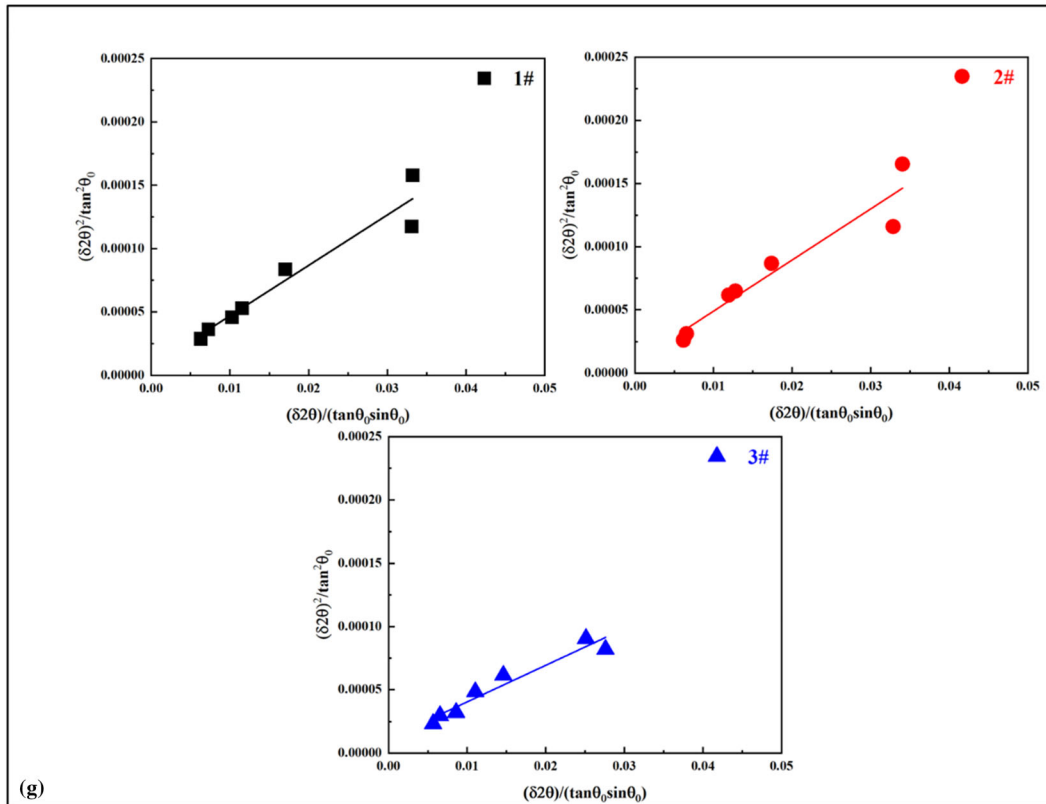
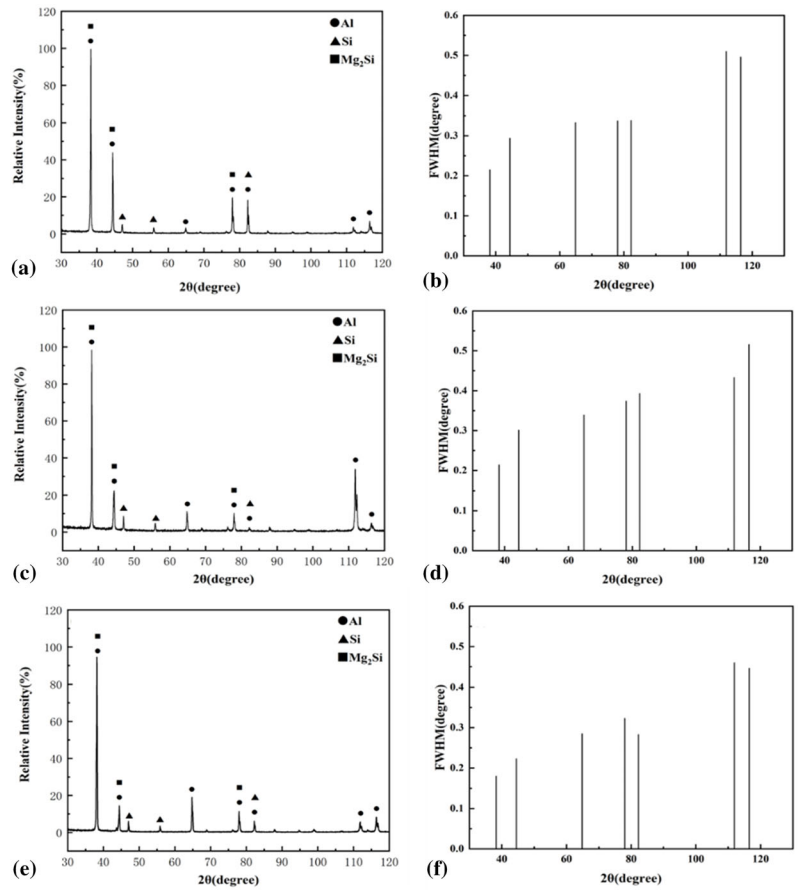


**Fig. 2** XRD patterns and half-peak width maps of three kinds of samples: (a, b) 1#, (c, d) 2#, (e, f) 3#, and the linear fitting relations of  $(\delta 2\theta)^2 / \tan^2 \theta_0$  and  $\delta 2\theta / \tan \theta_0 \sin \theta_0$ : (g)

**Table 2** The calculation parameters of dislocation density of Al-Si-Mg alloy samples with different aging temperatures

| Samples | $d$ , nm | $\langle e^2 \rangle^{1/2}$ | $\rho$ , ( $10^{14} \bullet \text{m}^{-2}$ ) | $\sigma_\rho$ , MPa |
|---------|----------|-----------------------------|--|---------------------|
| 1#      | 36.42    | 5.10E-04                    | 1.69   | 71.06               |
| 2#      | 34.47    | 5.37E-04                    | 1.89   | 75.01               |
| 3#      | 34.16    | 2.41E-04                    | 0.85   | 50.42               |

strengthening value of the alloy. The calculation formula of this model is illustrated in Eq 1 (Ref 12):

$$\frac{(\delta 2\theta)^2}{\tan^2 \theta_0} = \frac{\lambda}{d} \left( \frac{\delta 2\theta}{\tan \theta_0 \sin \theta_0} \right) + 2.5 \langle e^2 \rangle \quad (\text{Eq 1})$$

where  $(\delta 2\theta)$  represents the XRD half-width of the peaks;  $(\lambda)$  denotes the XRD diffraction Cu-K $\alpha$  radiation wavelength, taken as 0.15406 nm;  $(d)$  signifies the coherent XRD diffraction region size;  $(\theta_0)$  is the angle position of the main diffraction peak; and  $\langle e \rangle$  represents lattice strain.

Equation 1 depicts the relationship between  $(\delta 2\theta)^2 / \tan^2 \theta_0$  and  $\delta 2\theta / \tan \theta_0 \sin \theta_0$ , and by utilizing linear fitting to obtain the fitted slope and intercept (as shown in Fig. 2(g)), Eq 2 can be used to calculate the coherent XRD diffraction region size ( $d$ ), average lattice strain ( $\langle e^2 \rangle^{1/2}$ ), and dislocation density ( $\rho$ ) for each alloy sample (Ref 13):

$$\rho = \frac{2\sqrt{3}\langle e^2 \rangle^{1/2}}{(d \times b)} \quad (\text{Eq 2})$$

where  $(b)$  stands for the Burgers vector, taken as 0.286 nm. The dislocation density ( $\rho$ ) obtained using Eq 2 is used to calculate the dislocation strength ( $\sigma_\rho$ ) of each alloy through Eq 3 (Ref 14-16):

$$\sigma_\rho = M\alpha Gb\rho^{1/2} \quad (\text{Eq 3})$$

Here  $(M)$  is the Taylor factor with a value of 3.06;  $(\alpha)$  is the numerical factor, with a value of 0.204;  $(G)$  represents the shear modulus, valued at 26.9 GPa. Table 2 presents the numerical values of the dislocation density and dislocation strength for the three alloys.

The data in the Table 2 indicated that as the aging temperature increases, the dislocation density and dislocation strength of the three samples show a trend of initially increasing and then decreasing. Sample 1# exhibited a lower dislocation density and dislocation strength, measuring  $1.69 \times 10^{14} \bullet \text{m}^{-2}$  and 71.6 MPa, respectively. For sample 2#, the dislocation density and dislocation strength are  $1.89 \times 10^{14} \bullet \text{m}^{-2}$  and 75.01 MPa. Sample 3# showed a relatively lower value of dislocation density ( $0.85 \times 10^{14} \bullet \text{m}^{-2}$ ) and dislocation strength (50.42 MPa). This was attributed to the pinning effect caused by the precipitated second phase,  $\beta$  phase ( $\text{Mg}_2\text{Si}$ ), and spherical Si, affecting the dislocation movement, thus leading to strengthening and enhancement of the alloy's mechanical properties. Sample 1# displayed fewer precipitations of these two phases, resulting in less effective pinning of dislocation movement compared to sample 2#. Meanwhile, the existence of coarser rod-shaped  $\beta'$  precipitates in sample 3# further hindered the pinning effect on dislocation movement, thereby reducing the strengthening effect (Ref 17).

### 3.3 Intracrystalline Precipitates

Figure 3 presents the intracrystalline morphology and changes in the average size of precipitates in the three alloy samples under different aging temperatures. It could be observed that in sample 1#, the distribution of intracrystalline precipitates appears relatively uniform, and their sizes are generally smaller. Comparatively, in sample 2#, a trend toward needle-shaped precipitates was noticeable, and their sizes were larger than that of sample 1#. In term of sample 3#, the quantity of intracrystalline precipitates was reduced, accompanied by a slight increase in size. This phenomenon was attributed to the acceleration of precipitate growth at elevated aging temperatures (Ref 1), resulting in an increase in precipitate size.

Before the formation of GP zones, the decomposition of the supersaturated solid solution (SSS) began with the clustering and co-clustering of Mg and Si atoms (Ref 10). Subsequently, atomic segregation zones, known as GP zones, were formed. As aging progresses, these GP zones evolved into metastable transition phases  $\beta''$  and  $\beta'$ . With further aging treatments, the alloy developed a stable equilibrium phase  $\beta$  ( $\text{Mg}_2\text{Si}$ ) with independent lattices. Prolonged aging time led to over-aging, causing a decline in the alloy's strength and other mechanical properties (Ref 10).

Figure 4 displays the high-resolution transmission electron microscopy (HRTEM) images and corresponding fast Fourier transform (FFT) images of the alloy samples at different aging temperatures, with the electron beam incident direction along the  $\langle 100 \rangle_{\text{Al}}$  orientation. Figure 4(a) illustrates the HRTEM morphology of the GP zones in sample 1#, and the FFT pattern (Fig. 4(c)) revealed the complete coherency of GP zones with the Al matrix. Figure 4(d) and (e) presents the HRTEM morphology of the  $\beta''$  phase in sample 2#, exhibiting a distributed monoclinic structure, partially coherent with the matrix along the  $b$ -axis while semi-coherent along the  $a$ -axis and  $c$ -axis. In Fig. 4(e),  $a = 1.51$  nm,  $c = 0.67$  nm, and  $\beta = 105.26^\circ$ . Moreover, a significant presence of  $\beta''$  phase was observed within sample 2#, known as the most effective hardening phase (Ref 3), impacting the mechanical properties of the sample. Figure 4(g) and (h) illustrates the HRTEM morphology of the  $\beta'$  phase in sample 3#, while Fig. 4(i) represents the corresponding FFT image. With increasing aging temperature, the precipitate evolved into  $\beta'$  phase with larger size and a more structured arrangement. These sparsely distributed, coarser  $\beta'$  phases in sample 3# contributed to the deterioration of its mechanical properties (Ref 10).

### 3.4 Grain Boundary Precipitates

Figure 5 illustrates the grain boundary morphology of the alloy samples at three different aging temperatures. Figure 5(a) displays a scanning transmission electron microscopy (TEM) image of the grain boundary in sample 1#. It revealed a continuous and uniform distribution of grain boundary precipitates (GBPs) along the grain boundary. In Fig. 5(b), the TEM image of the grain boundary in sample 2# depicted a noticeable reduction in the quantity of precipitates at an aging temperature of 175 °C, accompanied by an increase in size and a discontinuous distribution along the grain boundary. Moving to Fig. 5(c), at an elevated aging temperature of 185 °C in sample 3#, there was an increase in both the quantity and size of the precipitates along the grain boundary, forming a continuous and uniform distribution. The observed width

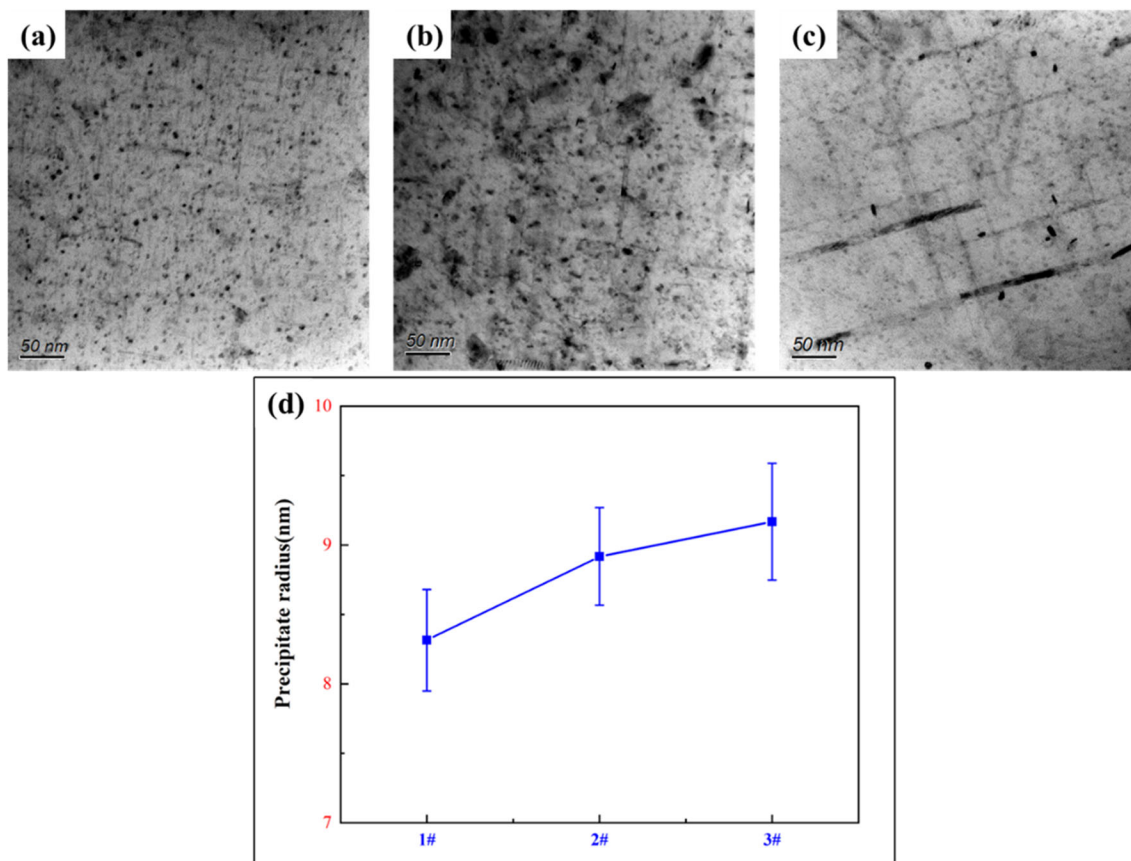


**Fig. 3** Intragranular TEM diagrams after different aging temperatures: (a) 1#; (b) 2#; (c) 3#, and the variation of average size of precipitates: (d)

variations of the precipitate-free zone (PFZ) at the grain boundaries across the three alloy samples were not distinctly significant. As inferred from Fig. 4, with increasing aging temperature, the evolution of precipitates progressed from GP zones to needle-like  $\beta''$  precipitates and further evolved into rod-shaped  $\beta'$  precipitates. The presence of  $\beta''$  phase might affect the diffusion and precipitation at the solute to grain boundary (Ref 6). Additionally, the discussion suggested that higher aging temperatures accelerate the growth of precipitates, leading to larger precipitate sizes. In aluminum alloys, grain boundary precipitates formed due to the decomposition of the saturated solid solution at grain boundaries, resulting in various precipitates, continuous distribution, and the generation of potential differences between the precipitates and the matrix, causing intergranular corrosion (Ref 15, 16). While GBPs generally had a minimal effect on the alloy's strength, they significantly impacted corrosion resistance and other properties. From Fig. 5, it was apparent that the GBPs in sample 2# exhibit a discontinuous distribution, implying a potential improvement in corrosion resistance compared to samples 1# and 3#.

### 3.5 Hardness and Electrical Conductivity

Figure 6 presents the hardness and electrical conductivity results obtained from the three alloy samples after different temperature aging treatments. Sample 1# displayed a hardness of 112.7 HV, while sample 2# exhibited a hardness of 118.8 HV, indicating a 5.13% increase compared to sample 1#. In contrast, sample 3# showed a hardness of 101.5 HV,

resulting in a 14.56% decrease compared to sample 2#. The hardness of all three samples initially increased and then decreased with rising aging temperatures. In the aging treatment of these alloy samples, supersaturated solid solutions decomposed to form needle-shaped precipitates, known as  $\beta''$  phase, as per the sequence of phase transformations during aging processes.  $\beta''$  phase was recognized as the most effective hardening phase (Ref 3). As observed in Fig. 4, the increase in aging temperature from 165 to 175 °C led to an augmentation in the quantity of needle-shaped precipitates, the  $\beta''$  phase, consequently causing an increase in hardness. However, as the aging temperature rose to 185 °C, the  $\beta''$  phase gradually evolved into a stable equilibrium phase,  $\beta$  phase, exhibiting an independent lattice structure. This evolution indicated an over-aging phenomenon, resulting in a decline in hardness as the distortion in the  $\alpha$ -Al matrix diminished.

It is well-known that electrical conductivity is determined by electron scattering caused by various disruptions within the crystal structure. This scattering is related to interactions between mobile electrons and localized strain fields generated by solute atoms, impurities, second-phase precipitates, grain boundaries, and dislocations (Ref 18). According to Matthiessen's rule (Ref 19), the total resistivity ( $\rho_t$ ) can be expressed as:

$$\rho_t = \rho_0 + \rho_{gb} + \rho_s + \rho_p + \rho_d + \rho_v \quad (\text{Eq 4})$$

Here,  $\rho_0$  represents the lattice resistivity of the Al matrix,  $\rho_{gb}$  is the grain boundary resistivity (Ref 20),  $\rho_s$  signifies the resistivity caused by solute atom dissolution into the matrix,  $\rho_p$  represents the resistivity caused by precipitated phases,  $\rho_d$  is the

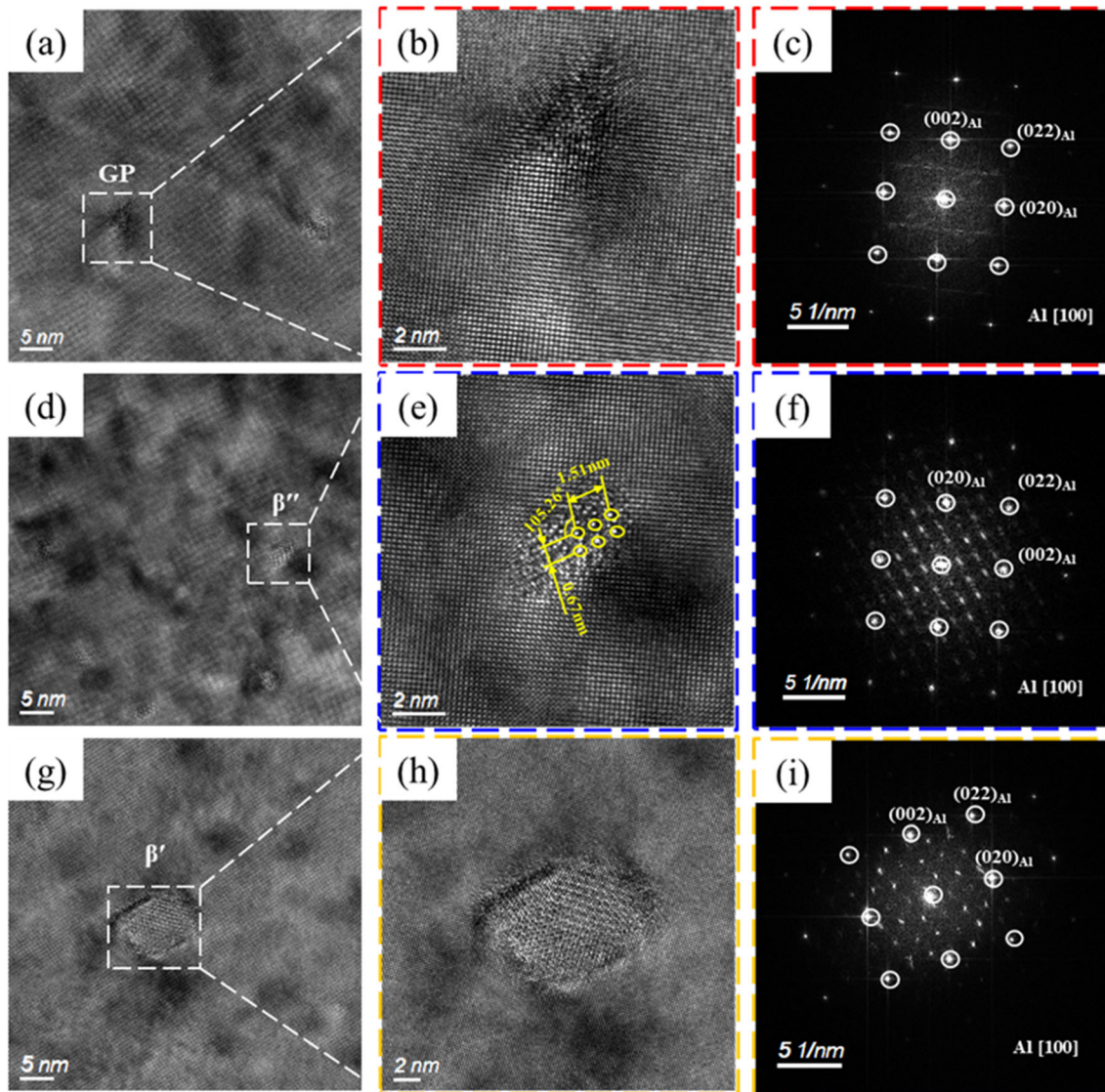


**Fig. 4** HRTEM diagram and corresponding FFT diagram after different aging temperatures: (a-c) 1#; (d-f) 2#; and (g-i) 3#

resistivity caused by dislocations, and  $\rho_V$  stands for vacancy-induced resistivity (Ref 4).

For a given alloy composition and the same grain structure, the Al matrix's lattice resistivity remains constant among the three alloy samples, while other resistivities vary with aging temperature. As per E.V. Bobruk's study (Ref 21), grain refinement to ultrafine scales could enhance the alloy's strength without sacrificing electrical conductivity. Therefore, the effect of grain boundary resistivity could be disregarded. Additionally, coarsening of precipitates in the alloy reduced electron scattering or the number of dissolved atoms, favoring improved electrical conductivity. Among  $\rho_p$ ,  $\rho_d$ ,  $\rho_V$ , the resistivity  $\rho_s$  caused by solute atom dissolution into the matrix could more effectively impact electron scattering (Ref 22). As observed in Fig. 1, at lower aging temperatures, the solute concentration was higher, with finer precipitates. With increasing aging temperature, the solute atom's supersaturation decreased, leading to an increase in precipitates, thereby reducing the solute atom content in the matrix and subsequently increasing electrical conductivity. As depicted in Fig. 6, the electrical conductivity of the samples rose with increasing aging

temperature. Specifically, sample 1# exhibited an electrical conductivity of 37.19 %IACS, while sample 2# showed 42.09 %IACS, marking a 13.18% improvement over sample 1#. Sample 3# displayed the highest electrical conductivity, reaching 44.39 %IACS, marking a 19.36% improvement over sample 1#. During aging, larger precipitates formed for longer times resulted in lower density larger precipitates, favoring increased electrical conductivity. Moreover, at higher aging temperatures, faster precipitation reduced the electron scattering caused by dissolved solute atoms, consequently enhancing electrical conductivity (Ref 23). These findings aligned with the analysis based on Matthiessen's rule.

### 3.6 Mechanical Properties

The mechanical properties and fracture features of the three alloy samples were evaluated through tensile testing, as shown in Fig. 7(a), which presents the specimen dimensions and stress-strain curves. The obtained tensile performance data for the three alloy samples after different temperature aging treatments are tabulated in Fig. 7(b). According to Fig. 7(b),

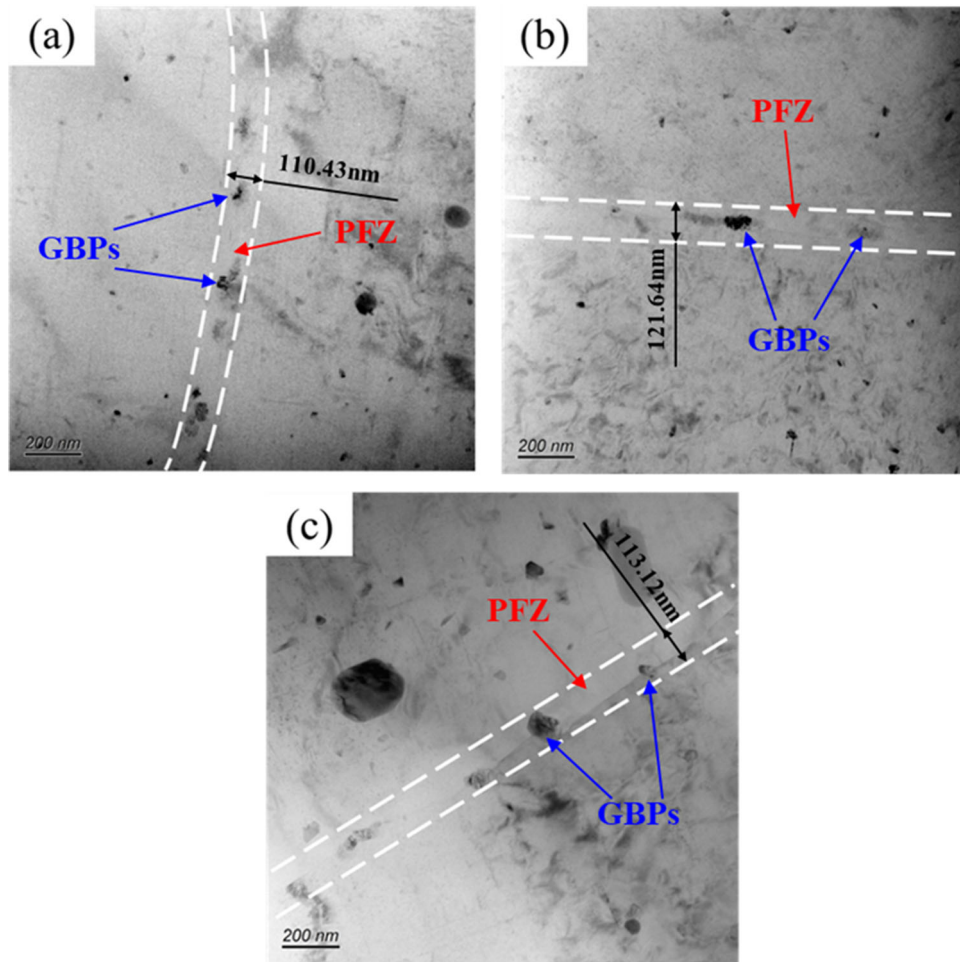


**Fig. 5** TEM diagram of grain boundaries at different aging temperatures: (a) 1#; (b) 2#; and (c) 3#

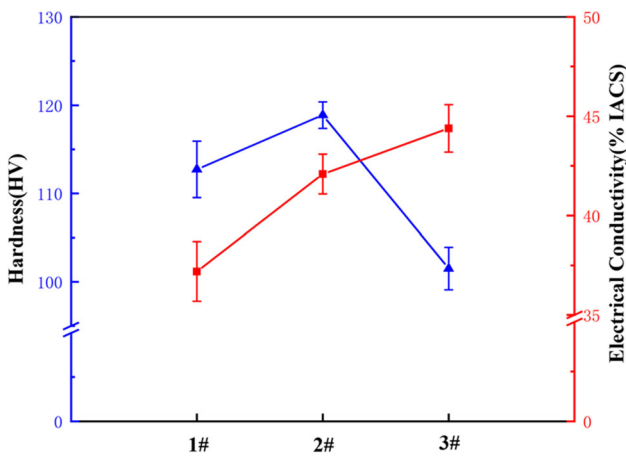


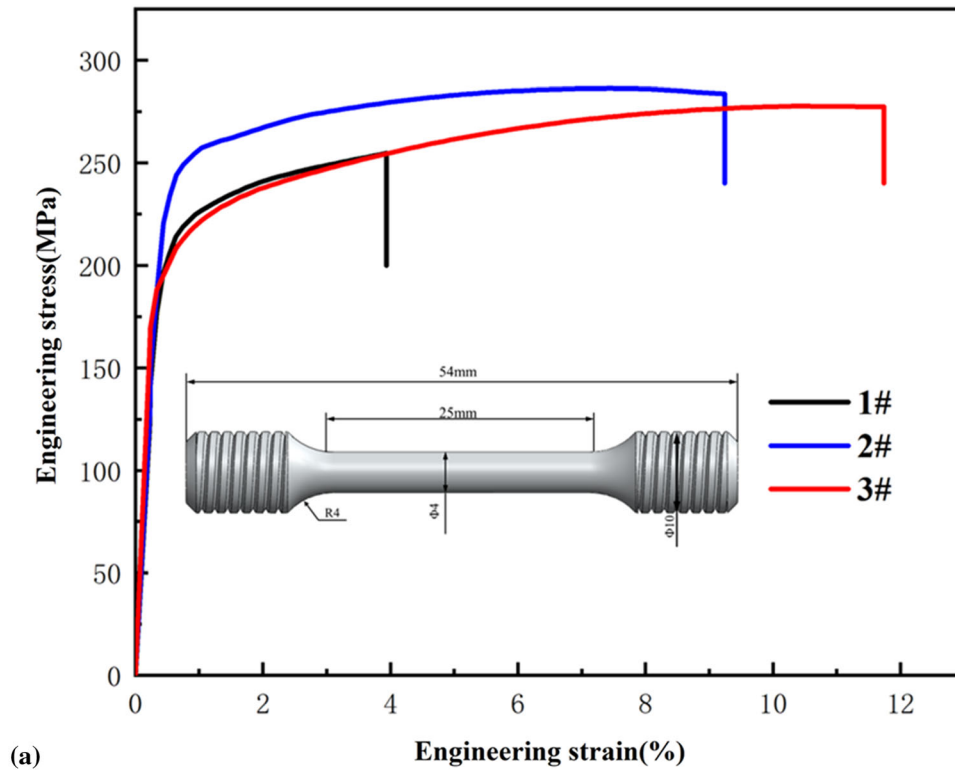
**Fig. 6** Hardness and conductivity of alloy specimens at different temperatures

sample 1# exhibited an ultimate tensile strength of 264.12 MPa and a yield strength of 222.67 MPa. Sample 2# displayed an ultimate tensile strength of 288.78 MPa and a yield strength of 259.38 MPa, showcasing a 9.33% increase in ultimate tensile strength and a 16.5% increase in yield strength compared to sample 1#. Meanwhile, sample 3# demonstrated an ultimate tensile strength of 280.78 MPa and a yield strength of

219.11 MPa, revealing a 2.77% decrease in ultimate tensile strength and a 15.5% decrease in yield strength relative to sample 2#. The tensile strength of the samples initially increased and then decreased with the increase in aging temperature. The enhancement of tensile properties after aging primarily resulted from the reprecipitation of solute atoms, increasing the quantity of second-phase particles that contributed to dispersion strengthening at grain boundaries. However, sample 1# aged at a lower temperature exhibited minimal second-phase precipitation, resulting in a weaker enhancement of tensile properties. At an aging temperature of 185 °C, the alloy developed coarser and sparsely distributed rod-shaped precipitates of the  $\beta'$  phase (Ref 10) (as depicted in Fig. 4(g)), which further transformed into a non-coherent stable equilibrium  $\beta$  phase, leading to strain loss around the precipitates (Ref 1) and weakening the strengthening effects of aging. Moreover, excessively high aging temperatures caused coarsening and enlargement of strengthening phases, which counteracted both aging and grain refinement strengthening. Hence, the trend observed in the tensile strength of the samples demonstrated an initial increase followed by a subsequent decrease as the aging temperature rises (Table 3).

Based on Fig. 7(b), it is evident that sample 1# exhibited a percent elongation at fracture of 3.52%, sample 2# displayed a percent elongation at fracture of 7.5%, and sample 3# showed a percent elongation at fracture of 10.72%. With the increase in





(a)

Tensile properties of Al-Si-Mg alloys at different aging temperatures

| Samples | Tensile Strength/MPa | Yield Strength/MPa | Elongation/% |
|---------|----------------------|--------------------|--------------|
| 1#      | 264.12±3.5           | 222.67±0.25        | 3.52±0.7     |
| 2#      | 288.78±3.26          | 259.38±0.14        | 7.5±0.5      |
| 3#      | 280.78±2.98          | 219.38±0.12        | 10.72±0.49   |

(b)

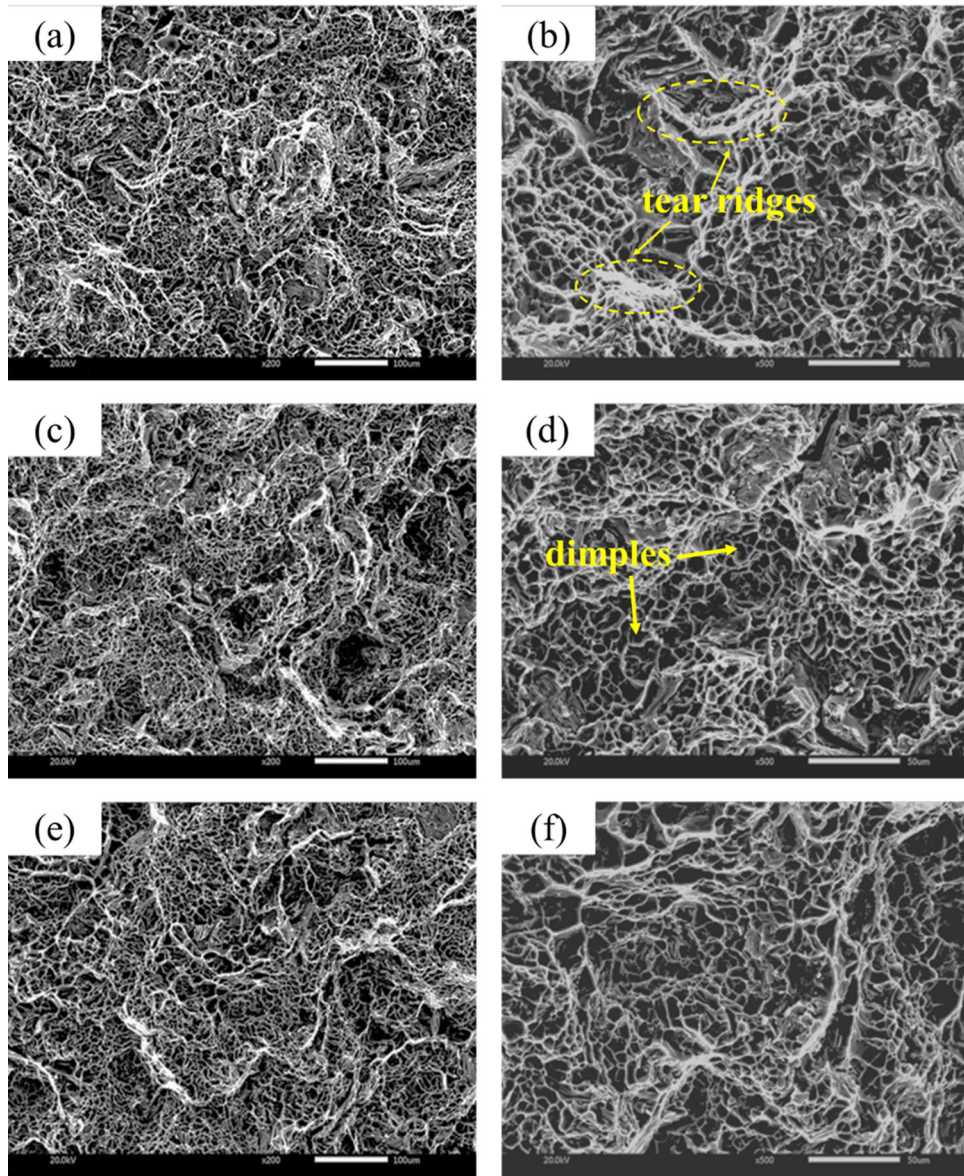
Fig. 7 Tensile specimen size and stress-strain curve of alloy specimens: (a) and tensile properties of Al-Si-Mg alloys at different aging temperatures: (b)

**Table 3 Maximum depth of intergranular corrosion**

| Samples | Maximum depth, $\mu\text{m}$ |
|---------|------------------------------|
| 1#      | 186.91 ± 3.88                |
| 2#      | 149.31 ± 3.85                |
| 3#      | 222.56 ± 4.26                |

aging temperature, there was a gradual improvement in the percent elongation at fracture of the alloy. The percent elongation at fracture was significantly influenced by the ability of Si particles in the Al-Si phase to impede dislocation movement. Aging treatments caused the eutectic Si particles in

the Al-Si-Mg alloy not only to spheroidize but also to distribute more uniformly in the microstructure (Ref 23, 24). The enhanced ability to impede dislocation movement resulted from the evenly distributed Si particles. Dislocations interacted with Si particles, piled up along the grain boundaries formed by Si particles at the fracture surface, leading to high elongation fractures (Ref 24). As the aging temperature rose, Si particles tended to diffuse more easily and spheroidize, and atomic diffusion rates increased, significantly reducing the quantity of residual intermetallic compounds. The reduction in the quantity of residual phases combined with the uniform distribution of Si particles collectively contributed to the increased elongation of the alloy (Ref 5).



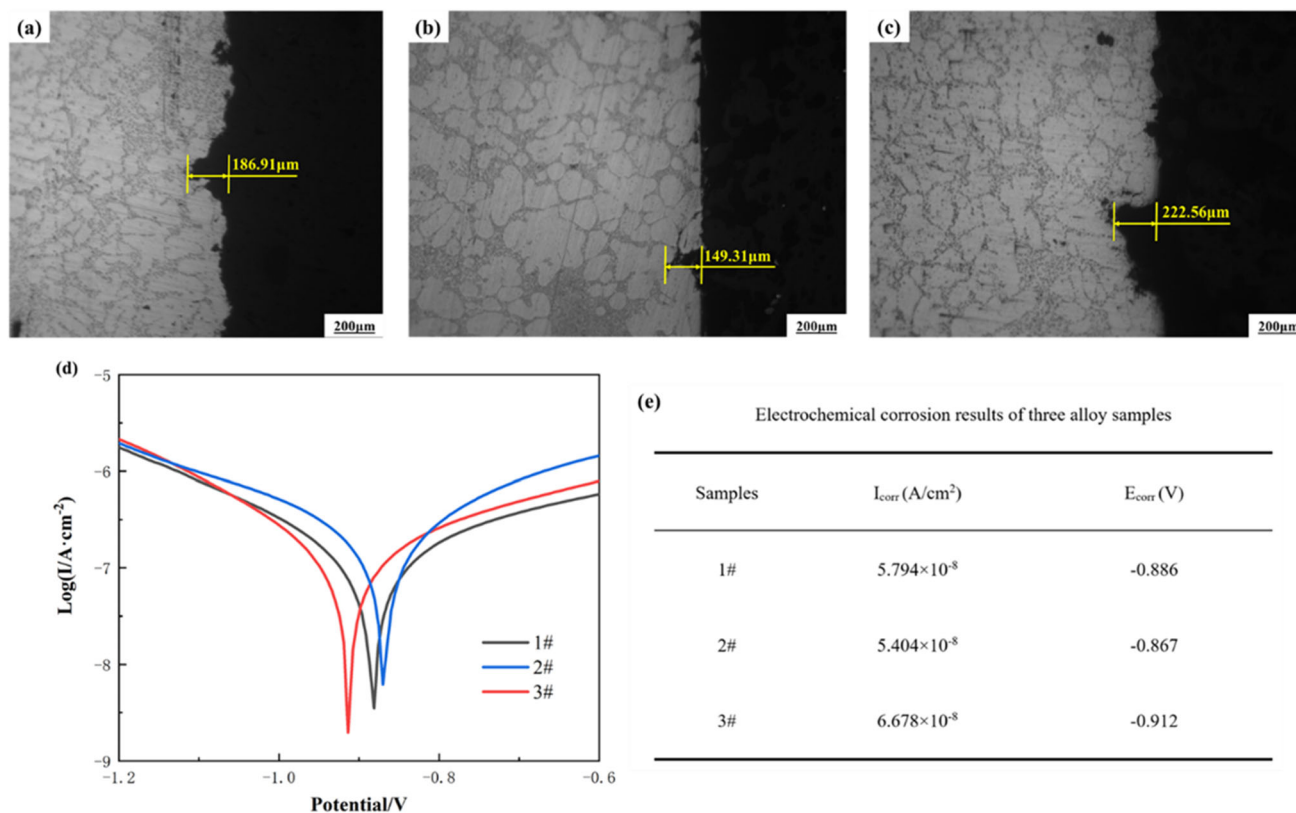
**Fig. 8** Fracture morphology of Al-Si-Mg alloy at different aging temperatures: (a, b) 1#; (c, d) 2#; and (e, f) 3#

Fig. 8 displays the fracture morphologies of the three alloy samples at magnifications of 200x and 500x under SEM. From Fig. 8(a) and (b), there were coarse and numerous tear ridges on the fracture surface, with deeply distributed and large dimples between these ridges. Reference (Ref 25) indicated that heterogeneous nucleation of intergranular precipitates leads to the formation and coalescence of micropores, causing the development of dimples in the intergranular fracture. Figure 8(c) and (d) displays the fracture morphology of sample 2#, which appeared relatively flat, exhibiting elongated tear ridges distributed across the fracture surface with large dimple areas. The fracture mode was transgranular fracture. Figure 8(e) and (f) reveals the fracture surface of sample 3#, which, although displaying coarse tear ridges, showed a more uniform distribution compared to samples 1# and 2#, furthermore, due to the enlarged Si particle distribution offering increased resistance to crack nucleation and propagation, promoting toughness in fracture (Ref 26). The formation of dimples primarily resulted from the separation of the matrix and Si phase during the tensile

process (Ref 5). With the rise in aging temperature, at 185°C, the Si particle distribution became more uniform, strengthening the ability of Si particles to impede dislocation movement within the Al-Si phase. Dislocations interacted with Si particles and accumulated at the grain boundaries formed on the fracture surface. Consequently, a significant amount of small dimples was observed in Fig. 8(f).

### 3.7 Corrosion Resistance

Corrosion between grains is the primary mode of corrosion propagation in artificial aging without Cu alloy (Ref 27). According to reference (Ref 28), the intergranular corrosion sensitivity of Al-Si-Mg alloy depended on the alloy composition and heat treatment conditions, where  $\beta$  ( $Mg_2Si$ ) phase precipitates at grain boundaries, resulting in intergranular corrosion. During the aging process, the solid solution formed in the solution treatment stage dissolves, simultaneously forming GP zones and segregating second phases (such as Si phase and  $\beta$  phase). These precipitates increased the potential



**Fig. 9** Corrosion morphology of alloy specimens at different aging temperatures: (a) 1#, (b) 2#, and (c) 3#; polarization curves of three alloy specimens (in 3.5 wt.% NaCl solution) (d) and electrochemical corrosion results of three alloy samples (e)

difference between different zones in the alloy, significantly deteriorating the corrosion resistance of the aged alloy. Figure 9(a) illustrates the intergranular corrosion morphology of sample 1#, with a maximum depth of 186.91  $\mu\text{m}$ . Figure 9(b) represents the intergranular corrosion morphology of sample 2#, displaying a maximum depth of 149.31  $\mu\text{m}$ , marking a reduction of 20.12% compared to sample 1#. As depicted in Fig. 5, under the aging temperature of 175  $^{\circ}\text{C}$ , the increased size of the GBPs resulted in reduced free energy, thereby slowing the corrosion rate and improving the alloy's corrosion resistance (Ref 29). However, with the rise in aging temperature, the aggregation and growth of  $\beta$  and Si phases intensified, leading to a deterioration in the alloy's corrosion resistance. Therefore, observing the intergranular corrosion morphology of sample 3#, with a maximum depth of 222.56  $\mu\text{m}$ , marking an increase of 49.06% compared to sample 2#.

The TEM images of intergranular precipitates at different aging temperatures shown in Fig. 5 revealed that, compared to the alloy specimens aged at 165  $^{\circ}\text{C}$  and 185  $^{\circ}\text{C}$ , the GBPs in the alloy aged at 175  $^{\circ}\text{C}$  displayed a discontinuous distribution, with relatively mild instances of continuous dissolution of the precipitates. Consequently, the extent of intergranular corrosion was minimized, indicating superior resistance to intergranular corrosion in the case of sample 2# among the tested specimens.

The polarization curves of the 1#, 2#, and 3# alloy specimens in a 3.5 wt.% NaCl solution are depicted in Fig. 9(d) and (e), presenting the corrosion potential ( $E_{\text{corr}}$ ) and corrosion current density ( $I_{\text{corr}}$ ). The findings indicated a trend of initially decreasing and then increasing  $E_{\text{corr}}$  and  $I_{\text{corr}}$  values with increasing aging temperature, with sample 2#

exhibiting the lowest corrosion current density and corrosion potential among the three alloy specimens. A higher  $I_{\text{corr}}$  correlated with increased corrosion rates, signifying inferior corrosion resistance in the alloy. The  $E_{\text{corr}}$  value reflected the likelihood and trend of corrosion in the alloy (Ref 30). A comprehensive analysis of the polarization curves, corrosion potential, and corrosion current density suggested that, relative to aging temperatures of 165  $^{\circ}\text{C}$  and 185  $^{\circ}\text{C}$ , the alloy Al-9Si-0.4Mg-Sr-Zr-Ti-Ce aged at 175  $^{\circ}\text{C}$  demonstrated the highest corrosion resistance, consistent with the intergranular corrosion experimental results.

Apart from the influence of the distribution of GBPs on the corrosion performance as mentioned earlier, existing literatures (Ref 31) have highlighted that the investigation of the electrochemical corrosion behavior of Al-Si-Mg alloys predominantly revolved around analyzing the impact of two elements, Mg and Si, along with the metallic intermetallic compounds they formed. Specifically, the presence of the metallic intermetallic compound magnesium silicide ( $\text{Mg}_2\text{Si}$ ) not only affected various mechanical properties of the alloy but also impacted its corrosion behavior in humid or chloride-ion environments. According to reference (Ref 31),  $\text{Mg}_2\text{Si}$  exhibited an anodic nature in comparison with the matrix, thus serving as the initiation site for corrosion. After the dissolution of  $\text{Mg}_2\text{Si}$ , it left behind a cavity, which acted as a nucleation site for pitting corrosion. Analyzing the results from the XRD analysis in Fig. 2 and the distribution of precipitates in the HRTEM images in Fig. 4, it was evident that the content and distribution of  $\text{Mg}_2\text{Si}$  and other metallic intermetallic compounds differed among the three alloy specimens. During experimentation in a 3.5 wt.% NaCl solution, the anodic

activity of Mg<sub>2</sub>Si intermetallic compounds rapidly decreased, leading to increased corrosion current density and a greater negative corrosion potential. Consequently, the alloy specimen 2# aged at 175 °C, exhibiting relatively lower Mg<sub>2</sub>Si content and a more dispersed distribution, demonstrated the best corrosion resistance among the three alloy specimens.

## 4. Conclusion

The present study investigated three distinct aging treatments (165 °C × 6 h, 175 °C × 6 h, 185 °C × 6 h) on Al-9.3Si-0.41Mg-0.2Zr-0.01Sr-0.08Ti-0.2Ce cast aluminum alloy. The study aimed to explore the influence of different aging temperatures on the microstructure and properties of the Al-9Si-0.41Mg-Sr-Zr-Ti-Ce cast aluminum alloy. The conclusions drawn from this investigation were as follows:

- (1) For the Al-9.3Si-0.41Mg-0.2Zr-0.01Sr-0.08Ti-0.2Ce alloy, the variation in the size of the second phase was not significant among the three aging temperatures (165 °C, 175 °C, and 185 °C). However, with increasing aging temperature, the distribution of precipitates became more diffuse, with a greater quantity and a tendency for localized precipitation in certain areas. The precipitated phases in the alloy included GP zones, β'' phase, β' phase, and β phase.
- (2) Different aging treatments significantly affected the comprehensive performance of the alloy. With rising aging temperatures, the hardness and tensile strength of the samples showed an initial increase followed by a decrease, while the elongation at fracture gradually increased. The alloy treated at 175 °C exhibited the best overall mechanical properties, with a hardness of 118.89 HV, a tensile strength of 303.15 MPa, and an elongation at fracture of 4.26%. The electrical conductivity increased gradually with aging temperature, and the electrical conductivity of sample 3# was the highest at 44.39% IACS.
- (3) The corrosion resistance of the three alloy samples exhibited an initial increase followed by a decrease with increasing aging temperature. The samples aged at 175 °C displayed the best corrosion resistance, with a corrosion current density of  $5.4036 \times 10^{-8}$  A/cm<sup>2</sup>, and a corrosion potential of -0.867 V. These findings were linked to the distribution of intergranular precipitates and the content and distribution of intermetallic compounds.

## Acknowledgments

The authors would like to thank Dr. Xiaojing Xu for his help in the experiment.

## Authors Contributions

Qin Wang contributed conceptualization, methodology, validation, writing—original draft, writing—review and editing, and formal analysis. Qingshan Zhou was involved in investigation and

writing—review and editing. Lele Liu was performed resources, formal analysis, and writing—review and editing. Xiaojing Xu was done supervision, conceptualization, resources, formal analysis, writing—review and editing, and visualization.

## Funding

Thanks to the financial support from the Key Projects of Equipment Pre-research Foundation of the Ministry of Equipment Development of the Central Military Commission of China (No:6140922010201) and the Key Projects of Research and Development of Zhenjiang (GY2018021).

## Data availability

The data used to support the findings of this study are available from the corresponding author upon request.

## Conflict of interest

The authors declare that they have no known competing financial interests or personal relationships that could have appeared to influence the work reported in this paper.

## References

1. H.R. Ammar, A.M. Samuel, F.H. Samuel, and A.M.A. Al-Ahmari, Aging Behavior of 359-Type Al-9%Si-0.5%Mg Casting Alloys, *J. Mater. Sci.*, 2011, **47**(3), p 1331–1338.
2. B. Rinderer, M. Couper, X.Y. Xiong, S.X. Gao, and J.F. Nie, Precipitation Sequence in an Al-Si-Mg Foundry Alloy, *Mater. Sci. Forum*, 2010, **654–656**, p 590–595.
3. R. Chen, Q. Xu, H. Guo, Z. Xia, Q. Wu, and B. Liu, Modeling the Precipitation Kinetics and Tensile Properties in Al-7Si-Mg Cast Aluminum Alloys, *Mater. Sci. Eng. A*, 2017, **685**, p 403–416.
4. P.K. Rout, M.M. Ghosh, and K.S. Ghosh, Microstructural, Mechanical and Electrochemical Behaviour of a 7017 Al-Zn-Mg Alloy of Different Tempers, *Mater. Charact.*, 2015, **104**, p 49–60.
5. X. Yan, X. Xu, Q. Zhou, and Z. Sun, Effect of Solid Solution System on the Properties of Al-6.5Si-5.5Cu-0.2Zr-0.01Sr-0.06Ti-0.2Ce Alloy in the Aging State, *J. Mater. Eng. Perform.*, (2023)
6. K.A. Unocic, P. Kobe, M.J. Mills, and G.S. Daehn, Grain Boundary Precipitate Modification for Improved Intergranular Corrosion Resistance, *Mater. Sci. Forum*, 2006, **519–521**, p 327–332.
7. G. Sha, H. Möller, W.E. Stumpf, J.H. Xia, G. Govender, and S.P. Ringer, Solute Nanostructures and Their Strengthening Effects in Al-7Si-0.6Mg Alloy F357, *Acta Mater.*, 2012, **60**(2), p 692–701.
8. Y. Wang, Y. Lu, S. Zhang, H. Zhang, H. Wang, and Z. Chen, Characterization and Strengthening Effects of Different Precipitates in Al-7Si-Mg Alloy, *J. Alloys Compd.*, 2021, **885**, p 161028.
9. H.J. Kang, J.Y. Park, Y.S. Choi, and D.H. Cho, Influence of the Solution and Artificial Aging Treatments on the Microstructure and Mechanical Properties of Die-Cast Al-Si-Mg Alloys, *Metals*, 2021, **12**(1), p 71.
10. L. Yang, D. Bai, D. Wang, C. Liu, S. Yang, and G. Huang, Effect of Aging Temperature on Microstructure and Corrosion Behavior of 6082 Aluminum Alloy, *Mater. Today Commun.*, 2023, **36**, p 106583.
11. V. Fallah, B. Langelier, N. Ofori-Opoku, B. Raecisia, N. Provatias, and S. Esmacili, Cluster Evolution Mechanisms During Aging in Al-Mg-Si Alloys, *Acta Mater.*, 2016, **103**, p 290–300.
12. K.M. Youssef, R.O. Scattergood, K.L. Murty, and C.C. Koch, Nanocrystalline Al-Mg alloy with ultra-high Strength and Good Ductility, *Scripta Mater.*, 2006, **54**(2), p 251–256.
13. Y.H. Zhao, X.Z. Liao, Z. Jin, R.Z. Valiev, and Y.T. Zhu, Microstructures and Mechanical Properties of ultrafine Grained 7075 Al Alloy Processed by ECAP and Their Evolutions During Annealing, *Acta Mater.*, 2004, **52**(15), p 4589–4599.

14. X. Kai, Z. Li, G. Fan, Q. Guo, Z. Tan, W. Zhang, Y. Su, W. Lu, W.-J. Moon, and D. Zhang, Strong and Ductile Particulate reinforced Ultrafine-Grained Metallic Composites Fabricated by Flake Powder Metallurgy, *Scripta Mater.*, 2013, **68**(8), p 555–558.
15. D.S. Prasad, C. Shoba, and N. Ramanaiah, Investigations on Mechanical Properties of Aluminum Hybrid composites, *J. Market. Res.*, 2014, **3**(1), p 79–85.
16. M. KarbalaeiAkbari, H.R. Baharvandi, and O. Mirzaee, Nano-sized aluminum oxide reinforced commercial casting A356 alloy matrix: evaluation of hardness, wear resistance and compressive strength focusing on particle distribution in aluminum matrix, *Compos. Part B Eng.*, 2013, **52**, p 262–268.
17. J. Buha, R.N. Lumley, and A.G. Crosky, Precipitation and solute distribution in an Interrupted-aged Al-Mg-Si-Cu alloy, *Phil. Mag.*, 2008, **88**(3), p 373–390.
18. D. Jiang, Y. Liu, S. Liang, and W. Xie, The Effects of Non-isothermal Aging on the Strength and Corrosion Behavior of Al Zn Mg Cu Alloy, *J. Alloy. Compd.*, 2016, **681**, p 57–65.
19. A. Matthiessen and C. Vogt, On the Influence of Temperature on the Electric Conducting-Power of Alloys, *J. Power. Sources*, 2013, **243**(4311), p 603–610.
20. L. Liu, J. Jiang, B. Zhang, W. Shao, and L. Zhen, ENHANCEMENT of Strength and Electrical Conductivity for a Dilute Al-Sc-Zr Alloy via Heat Treatments and Cold Drawing, *J. Mater. Sci. Technol.*, 2019, **35**(6), p 962–971.
21. E.V. Bobruk, M.Y. Murashkin, V.U. Kazykhanov, and R.Z. Valiev, Aging Behavior and Properties of Ultrafine-Grained Aluminum Alloys of Al-Mg-Si System, *Rev. Adv. Mater. Sci.*, 2012, **31**(2), p 109–115.
22. M.Y. Murashkin, I. Sabirov, V.U. Kazykhanov, E.V. Bobruk, A.A. Dubravina, and R.Z. Valiev, Enhanced mechanical Properties and Electrical Conductivity in Ultrafine-Grained Al Alloy Processed via ECAP-PC, *J. Mater. Sci.*, 2013, **48**(13), p 4501–4509.
23. G. Lin, Z. Zhang, H. Wang, K. Zhou, and Y. Wei, Enhanced Strength and Electrical Conductivity of Al-Mg-Si Alloy by Thermo-Mechanical Treatment, *Mater. Sci. Eng. A*, 2016, **650**, p 210–217.
24. E. Sjölander and S. Seifeddine, Artificial Ageing of Al-Si-Cu-Mg Casting Alloys, *Mater. Sci. Eng. A*, 2011, **528**(24), p 7402–7409.
25. A.K. Vasudévan and R.D. Doherty, Grain Boundary Ductile Fracture in Precipitation Hardened Aluminum Alloys, *Acta Metall.*, 1987, **35**(6), p 1193–1219.
26. D.K. Dwivedi, R. Sharma, and A. Kumar, Influence of Silicon Content and Heat Treatment Parameters on Mechanical Properties of Cast Al-Si-Mg Alloys, *Int. J. Cast Met. Res.*, 2006, **19**(5), p 275–282.
27. S.K. Kairy, P.A. Rometsch, C.H.J. Davies, and N. Birbilis, On the Intergranular Corrosion and Hardness Evolution of 6xxx Series Al Alloys as a Function of Si: Mg Ratio, Cu Content, and Aging Condition, *Corrosion*, 2017, **73**(10), p 1280–1295.
28. T. Onda, Y. Hirano, and T. Doko, *Effect of Mg and Si Addition on the Intergranular Corrosion of Aluminum Alloy*, in: Sae Automotive Corrosion & Prevention Conference & Exposition, (1993)
29. P. Chen, L.H. Liang, G. Luo, and J.M. Zeng, Relationship Between Heat Treatments and Corrosion of Al-Si-Mg Casting Alloy, *Adv. Mater. Res.*, 2014, **900**, p 96–99.
30. C. Li, X. Xu, H. Chen, V. Tabie, J. Cai, Y. Liu, Z. Liu, and C.-T. Peng, Effect of Zn/Mg Ratio on Microstructure and Properties of Cold Extruded Al-xZn-2.4Mg-0.84Cu-0.2Zr-0.25Ti Aluminum Alloy, *J. Mater. Eng. Perform.*, 2020, **29**(10), p 5787–5795.
31. R. Escalera-Lozano, M.I. Pech-Canul, M.A. Pech-Canul, M. Montoya-Davila, and A. Uribe-Salas, The Role of Mg<sub>2</sub>Si in the Corrosion Behavior of Al-Si-Mg Alloys for Pressureless Infiltration, *Open Corros. J.*, 2010, **3**(1), p 73–79.

**Publisher's Note** Springer Nature remains neutral with regard to jurisdictional claims in published maps and institutional affiliations.

Springer Nature or its licensor (e.g. a society or other partner) holds exclusive rights to this article under a publishing agreement with the author(s) or other rightsholder(s); author self-archiving of the accepted manuscript version of this article is solely governed by the terms of such publishing agreement and applicable law.